

An Assessment of Water Color for Inland Water in China Using a Landsat 8-Derived Forel–Ule Index and the Google Earth Engine Platform

Xidong Chen , Liangyun Liu , Xiao Zhang , Junsheng Li , Shenglei Wang, Dong Liu, Hongtao Duan , and Kaishan Song 

Abstract—Water color is an important parameter in water quality assessment. However, the existing water color investigations have mostly focused on the lakes with areas greater than 1 km^2 . In order to improve the understanding of the color of water bodies in China, a cloud-free composite image of China for the summer of 2015 was generated using time-series of Landsat-8 imagery and the best-available-pixel (BAP) compositing algorithm. Then, the first Forel–Ule index (FUI) water color product with a resolution of 30 m was produced for China using the generated BAP composite and the Google Earth Engine computing platform. Finally, the first national-scale assessment of the FUI of natural lakes with an area $>0.01 \text{ km}^2$ ($N = 60026$) was conducted based on the generated FUI product. The generated FUI product was shown to have a high degree of consistency with *in situ* water surface reflectance-derived FUI ($R^2 = 0.90, P < 0.001$). Also, it had a high degree of consistency with the *in situ* Secchi depth ($R^2 = 0.90, P < 0.001$) and trophic level index ($R^2 = 0.62, P < 0.001$) datasets. In addition, we found that the most prevalent lake colors in China were yellow (about 49%) and green (about 41%). Besides, the proportion of small lakes (areas $< 1 \text{ km}^2$) found to be yellow was much larger than for large lakes (area $\geq 1 \text{ km}^2$) (50% against 28%). Our results will provide important information that can be used for preserving and restoring inland water resources.

Index Terms—China, Forel–Ule index (FUI), Google earth engine, inland water color, lake, Landsat 8.

Manuscript received January 15, 2021; revised May 11, 2021; accepted May 26, 2021. Date of publication June 1, 2021; date of current version June 17, 2021. This work was supported in part by the Strategic Priority Research Program of the Chinese Academy of Sciences under Grant XDA19090125, in part by the Key Research Program of the Chinese Academy of Sciences under Grant ZDRW-ZS-2019-1, in part by the National Natural Science Foundation of China under Grant 41825002, and in part by the National Natural Science Foundation of China under Grant 41971318. (Corresponding author: Liangyun Liu.)

Xidong Chen is with the Aerospace Information Research Institute, Chinese Academy of Sciences, Beijing 100094, China, and also with the University of Chinese Academy of Sciences, Beijing 100049, China (e-mail: chenxd@radi.ac.cn).

Liangyun Liu, Xiao Zhang, Junsheng Li, and Shenglei Wang are with the Aerospace Information Research Institute, Chinese Academy of Sciences, Beijing 100094, China (e-mail: liuly@radi.ac.cn; zhangxiao@radi.ac.cn; lijs@radi.ac.cn; wangsl@radi.ac.cn).

Dong Liu and Hongtao Duan are with the Key Laboratory of Watershed Geographic Sciences, Nanjing Institute of Geography and Limnology, Chinese Academy of Sciences, Nanjing 210008, China (e-mail: dliu@niglas.ac.cn; htduan@niglas.ac.cn).

Kaishan Song is with the Northeast Institute of Geography and Agroecology, Chinese Academy of Sciences, Changchun 130102, China (e-mail: songkaishan@iga.ac.cn).

Digital Object Identifier 10.1109/JSTARS.2021.3085411

I. INTRODUCTION

INLAND water bodies have a direct interface with human society and are important to the food supply, commerce, transportation, and human health [1]. However, with the growth of the population and the rapid development of the economy, China has been facing increasingly severe water scarcity and security issues in recent years [2]–[5]. Because of the close relationship between water bodies and humans, water bodies in China are under great pressure due to human activities and associated environmental changes [6]–[8]. According to the latest national survey results, the quality of 22.1% of all the inland water in China is classed as bad [4]. The severe pollution of inland water resources has further exacerbated the shortage of fresh water [6], [7]. Therefore, there is an urgent need to improve knowledge about the quality of water bodies to assist in the restoration and management of water resources in China.

Water quality is a comprehensive descriptor of the condition of a water body, including its chemical, biological, radiological, and physical properties [9]–[11]. Traditionally, water quality was assessed by *in situ* sampling and laboratory analysis [2], [12]. However, such *in situ* measurement is time-consuming and labor-intensive and is not suitable for large-scale investigations [13]. Nowadays, with the development of remote sensing technologies, satellite images offer an important source of information for monitoring different optical components in water [2], [3], [14]–[19]. In addition, because of their low cost and wide coverage, remote sensing technologies provide potential opportunities for regional, and large-scale water quality assessment [11]. The spectral signatures of water captured by remote sensing sensors can be used to retrieve different water quality measures, such as the suspended matter and colored dissolved organic matter content, the Secchi depth (SD), and the chlorophyll-a concentration [16], [17], [20], [21]. However, because most of these measures are physical, biological, or chemical parameters, the methods used to retrieve these parameters depend on the optical properties of inland water bodies [2], [22]–[24]. Since the optically active substances in inland water bodies are complex and variable, the use of these water quality retrieval methods is restricted to specific remote sensing sensors and environments [2], [4], [22], [23], [25], [26].

Water color is the result of interactions between sunlight and materials in the water, and is determined by the absorption and

scattering of various water components [3]. Due to its close relationship with the concentration of optically active materials in the water, water color is also regarded an important parameter for reflecting water quality [2], [27]–[29]. The earliest quantitative method used to determine water color involved the measurement of the Forel–Ulrich index (FUI) of water using the Forel–Ulrich color scale [30], [31]. The FUI divides water into 21 levels, ranging from dark blue to yellowish brown [32]. Since the FUI is an optical parameter, it can be directly derived from optical satellite imagery using invariant formulas, and its use is not restricted to certain seasons or regions [2], [14], [33]. In addition, because the FUI covers a very wide range of optical characteristics of natural water bodies, it can be used to assess the water color of a wide range of water bodies [32], [34], [35]. Recently, the FUI has also been found to be closely related to the SD and trophic state of inland waters [23], [36]. Because of the above advantages, FUI has become as an important optical parameter for water quality assessment in recent years [23], [27], [32]. Since FUI can reflect water quality, and the retrieval of FUI is not seriously affected by the spatial and temporal variations in the optical properties of inland water bodies, it is feasible to use FUI in the large-scale monitoring of the quality of inland water bodies.

In recent years, a number of studies have included investigations of water color in China. For instance, Li *et al.* [2] assessed the water color of the 10 biggest lakes in China. Wang *et al.* [3] evaluated the color of Lake Taihu from 2006 to 2007. Wang *et al.* [36] developed the 500-m FUI water color products of lakes with areas greater than 25 km^2 covering the period from 2000 to 2017. However, these investigations mostly focused on the color of lakes with areas greater than 1 km^2 and neglected the color of small water bodies (area $< 1 \text{ km}^2$) [2], [4], [37]. As the number of different types of water quality investigations increases, there is an increasing need for a comprehensive understanding of the color of water bodies in China [2]. However, monitoring the color of water bodies with different areas requires high-resolution water color products, and there is still a lack of fine-resolution water color products for China.

In order to support the protection and management of water bodies in China, the aims of this study were i) to develop the first 30-m FUI water color product for China, and ii) to provide the first assessment of the water quality for 60026 lakes in China with areas larger than 0.01 km^2 . Taking into account the huge amount of computation and storage space required for national-scale water color mapping, the high-performance Google Earth Engine (GEE) cloud-based platform [38] was used to support the computation. The results of our study will provide useful guidance for the preservation and restoration of water resources.

II. DATASETS

A. Datasets Remote Sensing Datasets

In this article, Landsat-8 Operational Land Imager (OLI) data were collected from the GEE platform to generate the FUI water color product of China. Since the biomass of planktonic algae generally peaks in summer and the water state is relatively stable at this time, summer is considered to be the best season for assessing the quality of inland water bodies [39]–[41]. However,

because of the long revisit periods of Landsat data and the frequent contamination of cloud in images, it is difficult to generate spatially continuous watercolor maps with only one year of data [42], [43]. Additional images were required in order to have sufficient cloud-free observations. Accordingly, the Landsat-8 surface reflectance (SR) data of China archived on GEE during the summer months (from June to September in the northern hemisphere [23]) of 2014 to 2016 were used to generate the FUI map for the nominal year of 2015. The SR images provided by GEE had been radiometrically corrected using the Landsat SR Code atmospheric correction algorithm [44]. In addition, cloud, shadow, water, and snow pixels were annotated in the quality assessment (QA) band of each image using CFMASK [45].

B. Auxiliary Inland Water Products

The 30-m dynamic inland water body map (DIWBM) of China [46] was used to extract water body regions. The DIWBM database was generated using more than 6000 Landsat 8 images acquired between January and December in 2015. The water bodies in the DIWBM were divided into intraannual permanent and seasonal water pixels according to the frequency of the occurrence of water. The water pixels with a frequency ≥ 0.9 were labeled as permanent water; the other water pixels were labeled as seasonal water [46]. The DIWBM has a high accuracy for both permanent and temporary water bodies. The user's accuracies are 98.36% and 92.53% and the producer's accuracies are 97.45% and 95.39% for permanent and temporary water, respectively. Since some temporary inland water bodies (such as paddy fields) have vegetation on the surface [46]–[48], the colors derived for these water bodies can differ from their natural colors. In order to remove the impact of this, the permanent water regions captured in the DIWBM were used to mask permanent water pixels.

In addition, the Chinese lake inventories for 2005 [49] and 2010 [50], the global lakes and wetland database (GLWD) [51], and the existing Chinese Reservoirs and Dams vector database [52] were used to assist in the extraction of lakes. The 2005 and 2010 Chinese lake inventories include lakes with areas $> 1 \text{ km}^2$ and $> 8 \text{ ha}$, respectively. The GLWD is a comprehensive database of global water containing reservoirs, lakes, and rivers with areas $\geq 0.1 \text{ km}^2$; the Chinese Reservoirs and Dams database includes reservoirs and dams with areas $> 8 \text{ ha}$.

Moreover, Wang *et al.* [23] developed FUI products for large lakes in China from 2000 to 2017 using 8-day MODIS images [36]. The MODIS-derived FUI products from June to September 2015 were collected for comparison with our Landsat 8-derived FUI data.

C. In Situ Data

Since the *in situ* FUI data is very limited, it is difficult to perform ground-based validation using the *in situ* FUI data. Fortunately, previous studies have shown that the FUI can be accurately calculated by using water SR [53]. To this end, some *in situ* water SR data measured in Yuqiao Reservoir and Guanting Reservoir concurrent to (± 7 days) our used Landsat 8 images

TABLE I

LOCATIONS WHERE THE *IN SITU* DATASETS WERE COLLECTED AND THEIR VALUES. THESE DATA INCLUDED 24 SD MEASUREMENTS AND 18 MONTHLY LAKE AVERAGE TLI VALUES

No.	Lat (N)	Long (E)	Date	SD (m)	Lake Name	Lake Center Lat (N)	Lake Center Long (E)	Date	TLI (lake average)
1	91.00	30.83	2014/8/17	10.0	Dianchi	102.72	24.87	2016/8	65.0
2	90.97	30.82	2014/8/17	10.0	Dianshan	120.97	31.12	2015/8	58.0
3	90.84	30.79	2014/8/18	12.0	Chaochu	117.60	31.54	2014/8	58.0
4	90.81	30.80	2014/8/18	12.0	Longgan	116.17	29.95	2016/8	48.0
5	90.54	30.61	2014/8/16	10.0	Yangcheng	120.82	31.44	2016/8	55.0
6	90.51	30.63	2014/8/16	10.0	Gaoyou	119.34	32.85	2015/8	51.0
7	88.89	31.82	2014/8/7	3.2	Nanyi	118.99	31.12	2016/8	53.0
8	90.82	28.85	2015/8/19	5.4	Weishan	117.25	34.62	2014/8	51.0
9	117.58	40.04	2015/8/12	0.8	Dongting	112.97	29.31	2014/8	50.6
10	117.61	40.03	2015/8/12	0.7	Dongping	116.21	35.99	2014/8	51.0
11	117.57	40.03	2015/8/12	0.8	Caizi	117.11	30.81	2014/8	48.0
12	117.56	40.06	2015/8/12	0.8	Futou	114.22	30.01	2014/8	46.0
13	117.52	40.06	2015/8/12	0.8	Wuchang	116.69	30.27	2014/8	43.0
14	117.52	40.04	2015/8/12	0.9	Luoma	118.23	34.10	2014/8	45.0
15	117.49	40.03	2015/8/12	0.8	Chenghai	100.67	26.55	2015/8	42.0
16	117.52	40.02	2015/8/12	0.8	Erhai	100.19	25.79	2015/8	40.0
17	117.58	40.04	2015/8/12	0.7	Qiandao	118.94	29.56	2015/8	29.0
18	117.61	40.03	2015/8/12	0.7	Lugu	100.79	27.72	2014/8	20.0
19	117.57	40.03	2015/8/12	0.8					
20	117.56	40.06	2015/8/12	0.9					
21	117.52	40.06	2015/8/12	0.9					
22	117.52	40.04	2015/8/12	0.9					
23	117.49	40.03	2015/8/12	0.8					
24	117.52	40.02	2015/8/12	0.8					

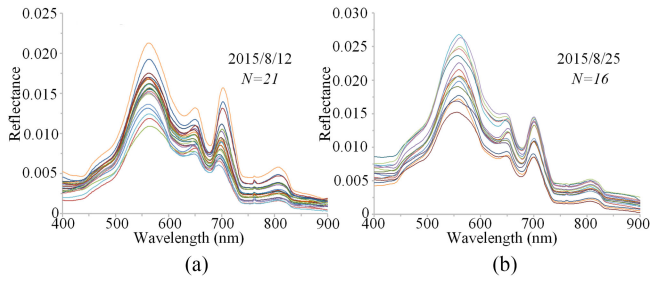


Fig. 1. *In situ* measured water SR datasets acquired in Yuqiao Reservoir ($N = 21$) and Guanting Reservoir ($N = 16$). The *in situ* reflectance in Yuqiao Reservoir were measured on 2015/8/12, and the *in situ* reflectance in Guanting Reservoir were measured on 2015/8/25.

were acquired from Wang *et al.* [36] to derive FUI for validation (see Fig. 1). The *in situ* reflectance dataset in Yuqiao Reservoir contained 21 samples and was measured on 2015/8/12, while the *in situ* reflectance data in Guanting Reservoir had 16 samples and were measured on 2015/8/25.

Recently, the FUI for inland water bodies was also demonstrated to have a strong correlation with the SD and trophic state [23], [35], [36], and there are many public *in situ* SD and trophic level index (TLI) [54] datasets. In order to increase the volume of *in situ* validation data, concurrent measured SD and TLI datasets were also acquired for use in validating our Landsat 8-derived FUI product (see Table I). The SD datasets were acquired from

Liu *et al.* [55] and Wang *et al.* [36], including a total of 24 samples. The time windows between these SD data and the Landsat acquisitions of the corresponding pixels were within ± 7 days. The TLI is an indicator of the trophic state [54], and can be collected from the website of the Ministry of Environmental Protection of China (<https://datacenter.mee.gov.cn/>). It should be noted that, the TLI data recorded in the Ministry of Environmental Protection of China were the monthly lake average TLI data. However, because some lakes in our FUI products were composed of pixels from different years and months, the average FUI of these lakes could not represent any specific time, and thus, no matching monthly TLI data could be found. Therefore, only when the acquisitions of pixels that make up the lake were from the same month and year, the lake was selected to calculate the lake average FUI and used for comparison with the matched *in situ* TLI data. As a result, a total of 18 lakes was selected, and the matching *in situ* TLI data were collected. The accuracy of our product is indirectly verified by analyzing the relationship between our FUI product and the collected *in situ* SD and TLI data.

III. METHOD

A flowchart representing how the 30-m inland water FUI map was generated is illustrated in Fig. 2. First, the annual cloud-free composite of China in the summer of 2015 was derived using the Landsat-8 time-series data and the best-available-pixel (BAP)

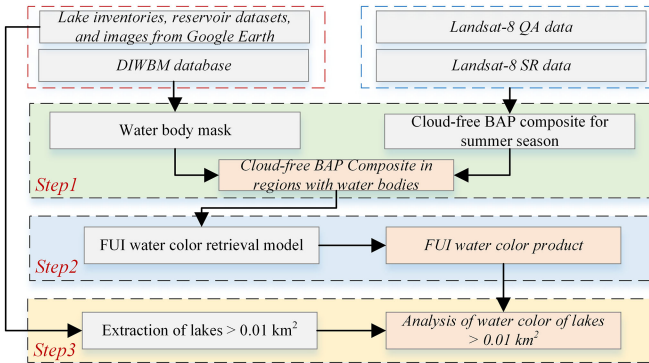


Fig. 2. Flowchart of the developed FUI water color product. Note: SR: surface reflectance; QA: Quality Assessment; DIWBM: the 30-m Dynamic Inland Water Body Map; BAP: best-available-pixel; FUI: Forel–Ulle index.

compositing algorithm. Meanwhile, water regions were masked in the BAP composite using the DIWBM database. Next, based on the generated BAP composite of inland water bodies, the first 30-m FUI water color product of China was developed using the GEE computing platform. Finally, the lakes with an area $>0.01 \text{ km}^2$ were extracted by making reference to the existing lake inventories, reservoir datasets, and high-resolution images in Google Earth. Finally, the first national-scale analysis of the FUI for lakes larger than 0.01 km^2 was conducted using the developed lake dataset and the generated FUI product.

A. Generation of Cloud-Free Composites in Regions With Water Bodies Using BAP Composition

Recently, White *et al.* [56] developed a BAP compositing algorithm to generate cloud-free composites over large areas. The BAP algorithm can generate phenologically consistent cloud-free composites for a time period of interest, and can flexibly change its rules to accommodate various information needs [56]–[58]. Many researchers have used this algorithm to generate seasonally constrained composites for different land-cover mapping applications [56], [59]–[63]. Therefore, the BAP was used in this article to generate the cloud-free composite for the summer of 2015 [64]. Four separate scores were calculated; these included the cloud and cloud shadow distance score, the atmospheric opacity score, the acquisition year score, and the day of year (DOY) of the acquisition score (see White *et al.* [56] for details). These scores were summed to derive the BAP score for each pixel, and the observation with the highest score was defined as the composite value for each pixel. Since the first three scores rules were not sensitive to geographic location and phenology and as the default parameter values for the three rules were derived through comprehensive experiments, the parameters values for the first three rules were set as the default values [56]. Meanwhile, the cloud and cloud shadow and also the atmospheric opacity information were derived from the Landsat-8 QA data. Regarding the acquisition DOY score, because our aim was to generate summer image composites, the central date (August 1) of the summer months (June to September) was selected as the target DOY. In addition, the

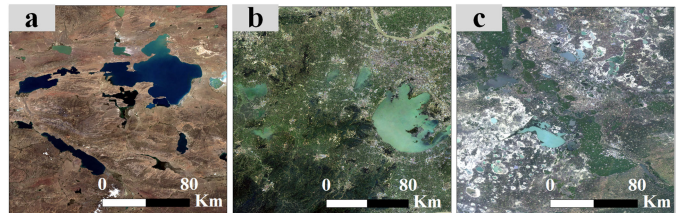
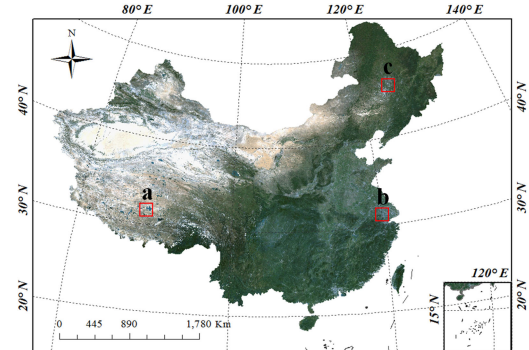


Fig. 3. 2015 annual cloud-free BAP composite of China. The enlargements show three typical areas containing water bodies.

standard deviation of the DOY was set to 60 to match the length of the summer window. The generated annual BAP composite for China is shown in Fig. 3. Enlargements of three typical regions that contain large numbers of water bodies are displayed in Fig. 3(a)–(c). It can be seen that the composite has good spatial continuity, and the details of the water boundaries and color are well described in our BAP composite.

Next, based on the water bodies delineated in the DIWBM, water pixels were extracted from the BAP composite. In order to mitigate the interference of aquatic vegetation, only the permanent water areas detected in the DIWBM were used for mapping. Since DIWBM has a high accuracy [46], the pixels flagged as corresponding to permanent water bodies in the DIWBM were selected as candidate water pixels in the generated BAP composite. Meanwhile, in order to minimize the effects of mapping error in DIWBM, the normalized difference water index (NDWI) [65] was used to refine the extracted candidate water pixels. If the NDWI of a candidate water pixel was lower than the lowest second quantile of the cumulative probability of all candidate water pixels (the threshold being based on the user's accuracy of 98.36% for DIWBM [46]), the candidate pixel was removed from the candidate water pixels.

B. Generation of the FUI Water Color Product

Based on the composited BAP data for water regions, the colors of the extracted water pixels were retrieved by calculating their FUI values. The derivation of the FUI was based on calculations of the commission on illumination's (CIE's) primary color "tristimulus" values (X , Y , Z), which specify the color stimulus of the human eye [14], [66]. The values of X , Y , and Z can be derived by integrating the reflectance spectrum and color matching functions over the visible light range (390–740 nm) [3], [67]. However, since Landsat 8 OLI imagery has only four bands (coastal, blue, green, and red) in the visible range, linear

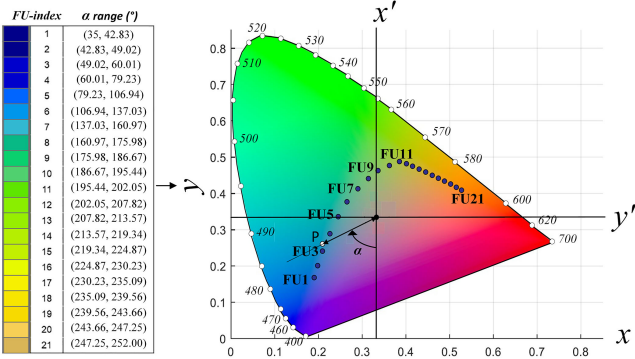


Fig. 4. 21-class FUI lookup table and the corresponding range of the hue angle, α , are shown on the left-hand side [23], [66]. The right-hand part of the figure shows the CIE chromaticity diagram with the (x , y) coordinates of the 21 FUI classes plotted as blue dots. An arbitrary spectrum is shown as point P, and the center of the chromaticity diagram is represented as point W ($x = y = z = 1/3$). The curved outer boundary is the spectrum of the monochromatic locus. Wavelengths are given in nanometers.

weighted sums [see (1)–(3)] of the band reflectances were used to estimate the tristimulus values [14], [37]

$$\begin{aligned} X &= 11.053 R(443) + 6.950 R(482) + 51.135 R(561) \\ &\quad + 34.457 R(655) \end{aligned} \quad (1)$$

$$\begin{aligned} Y &= 1.320 R(443) + 21.053 R(482) + 66.023 R(561) \\ &\quad + 18.034 R(655) \end{aligned} \quad (2)$$

$$\begin{aligned} Z &= 58.038 R(443) + 34.931 R(482) + 2.606 R(561) \\ &\quad + 0.016 R(655) \end{aligned} \quad (3)$$

where R is the reflectance at the relevant band.

Once X , Y , and Z had been derived, the color of a specific reflectance spectrum could be represented in the chromaticity diagram (see Fig. 4) [2], [23]. The chromaticity coordinates in the chromaticity diagram, x and y , were acquired by normalizing X , Y , and Z to the range 0–1

$$x = \frac{X}{X+Y+Z}, \quad y = \frac{Y}{X+Y+Z}. \quad (4)$$

Since the horseshoe-shaped envelope (locus) is derived from x and y values calculated from monochromatic light at each wavelength, the space enclosed by the locus encompasses all possible chromaticity values. The coordinates of the center point of the chromaticity diagram are $x = y = z = 1/3$, which represents the “white point”, W . As in the work of Wang *et al.* [3], the x and y coordinates of an upwelling radiance spectrum can be expressed by the hue angle (α), which is calculated using a new coordinate system (x' , y') (5). For ease of calculation, the angle α is defined as the angle between a line drawn from the “white point” to the x , y coordinates and the negative x' -axis; the angle is measured in a clockwise direction and thus has a positive value between 0° and 360° [23]. The angle α is derived from the four-quadrant arctangent function, ARCTAN2 (6) [23]

$$x' = y - 1/3, \quad y' = x - 1/3 \quad (5)$$

$$\alpha = \text{ARCTAN2} \left(\frac{x'}{y'} \right) * \frac{180}{\pi}. \quad (6)$$

However, due to the band settings of satellite sensors, there is an offset ($\Delta\alpha$) between the color perceived by the human eye and the color acquired by the sensor [33]. Fortunately, this offset is not completely random and can be approximately described using a polynomial equation. Following the method presented in van der Woerd and Wernand [14], Wang [68] developed a polynomial equation to model $\Delta\alpha$ for Landsat OLI data

$$\begin{aligned} \Delta\alpha &= 21.355b^5 - 199.29b^4 + 703.3b^3 - 1132.2b^2 \\ &\quad + 801.6b - 201.34. \end{aligned} \quad (7)$$

Here, b is 1% of the hue angle derived from (6). Using the calculated offset ($\Delta\alpha$), the hue angle α can be corrected to $\alpha + \Delta\alpha$. Finally, based on the corrected angle, α , the FUI can be retrieved using the 21-class FUI lookup table found in Novoa *et al.* [66] (see Fig. 4). The FUI value of a specific spectrum can be derived by finding the nearest FUI class to the corrected hue angle.

C. National-Scale Assessment of the Color of Lakes in China

In order to comprehensively analyze the spatial patterns in the color of water in Chinese lakes, lakes with an area $>0.01 \text{ km}^2$ were extracted in this article. First, the extracted water bodies (see Section III-A) were converted into polygonal vector objects using ArcMap. After this, the lake objects with an area $>0.01 \text{ km}^2$ (more than ten pixels) were extracted. Next, by referring to the Chinese lake inventories of 2005 [49] and 2010 [50], the lake vectors from the GLWD [51] and the high-resolution images from Google Earth, extracted water objects whose centroid pixels coincided with lake vectors in the Chinese lake inventories and the GLWD were labeled as lake objects. Then, the remaining unlabeled water objects were manually flagged as either lake or nonlake objects based on the high-resolution images from Google Earth. Finally, lakes whose centroid pixels coincided with reservoir and dam vectors in the Chinese Reservoirs and Dams vector database [52] were excluded. As a result, a total of 60026 lakes were extracted. These lakes were divided into eight groups based on area: the ranges used were 0.01 to 0.5 km^2 , 0.5 to 1 km^2 , 1 to 10 km^2 , 10 to 50 km^2 , 50 to 100 km^2 , 100 to 500 km^2 , 500 to 1000 km^2 , and more than 1000 km^2 .

Then, the average FUI value of each lake was calculated to assess the water color of lakes in China. The floating algae index (FAI), a robust index for detecting aquatic vegetation, was used to further mask aquatic vegetation pixels to calculate the average FUI value of lakes [69], [70]. According to the previous work [36], [71], pixels with $\text{FAI} > -0.002$ were determined as lake aquatic vegetation and were not used to calculate the average FUI of each lake. In addition, taking into account that the shallow near-shore pixels would also interfere with the water color of lake, the method used in Shen *et al.* [72] was employed to further avoid interference caused by the shallow near-shore pixels. They set a corresponding FUI threshold for each lake, and calculated the overall FUI of the lake by using only those pixels whose FUI was less than the corresponding threshold [72]. The FUI threshold for each lake was set as the value that was greater than the FUI value of 80% of the pixels of the whole lake [72]. Therefore, pixels with $\text{FAI} \leq -0.002$ and FUI less than the

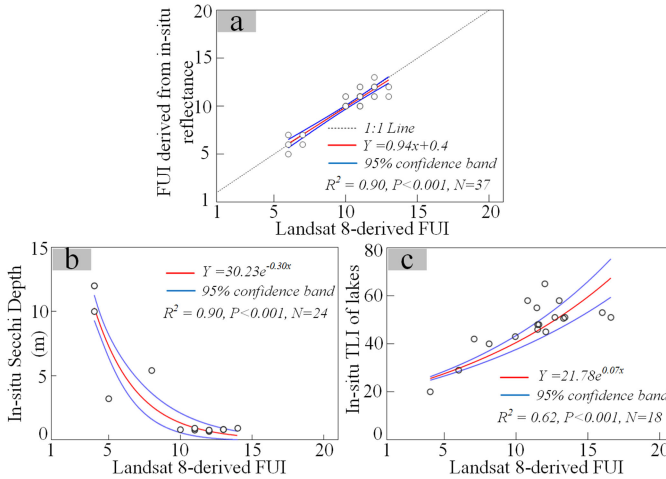


Fig. 5. Relationships between the FUI and the *in situ* measured datasets (see Section II-C). (a) Relationship between the Landsat 8-derived FUI and the *in situ* water SR-derived FUI; (b) Relationship between the FUI and SD; (c) Relationship between the FUI and TLI.

corresponding FUI threshold were used to calculate the average FUI of each lake.

Moreover, the method introduced by Li *et al.* [2] was also adopted to divide the lakes into four groups according to the overall FUI of the lakes: the groups were $1 \leq \text{FUI} < 6$, $6 \leq \text{FUI} < 9$, $9 \leq \text{FUI} < 13$, and $13 \leq \text{FUI} \leq 21$, corresponding to blue, cyan, green, and yellow water, respectively.

IV. RESULTS

A. Comparison of the Landsat 8-Derived FUI Product and the In Situ Measured Datasets

To validate our Landsat 8-derived FUI water color product, the relationship between our FUI product and the collected *in situ* water SR-derived FUI, the *in situ* SD, and the *in situ* TLI (see Section II-C) were analyzed. Fig. 5(a) shows the comparison of the FUI derived from the measured reflectance and the FUI derived from the concurrent Landsat 8 images, and it can be seen that all the scattered points are around the 1:1 line. A strong relationship is shown between the Landsat 8-derived FUI and the *in situ* water SR-derived FUI ($R^2 = 0.90$, $P < 0.001$). In addition, from Fig. 5(b) and (c), it can be seen that the relationship between SD and FUI can be well described by an exponential decay curve ($R^2 = 0.90$, $P < 0.001$), whereas there was a significant positive exponential relationship between TLI and FUI ($R^2 = 0.62$, $P < 0.001$). This is consistent with the results of previous studies [23], [36], [37]. The relationship between FUI and SD obtained in this article has a strong correlation with the relationship derived from Li *et al.* [2] ($r = 0.99$, $P < 0.001$), while the relationship between FUI and TLI shown in this article also shows a good correlation with the result derived from Chen *et al.* [37] ($r = 0.99$, $P < 0.001$). These results confirm the reliability of our developed FUI product. Moreover, because the SD and TLI are important indicators of water quality, it was also concluded that our derived FUI product can roughly indicate the water quality.

B. 30-m FUI Water Color Product for China

Fig. 6(a) shows the FUI water color product that was generated for China. It can be seen that the FUI values of the water bodies to the east of the famous Hu line [73] are higher than those of the water bodies to the west. The average FUI of the water bodies to the east of this line is greater than 12, whereas the average FUI for those to the west is about 10.5. In addition, the average FUI of the water bodies north of the Qinlin–Huaihe line (considered to be the dividing line between the north and south of China [74]) is about 11, whereas it is about 10.5 for the water bodies that lie to the south of this line. These results are consistent with the results of previous studies [23], [36], [72]. The retrieved colors of water bodies are shown in more detail for the three selected regions marked in Fig. 6(a): [see Fig. 6(b)–(d)]. Area b is located in Tibet and contains a large number of salt lakes; areas c and d are located in the Yangtze River Basin and the Ganjiang River Basin, respectively, and contain mainly freshwater lakes. It can be seen that there are more blue water bodies in area b than in areas c and d. The water bodies in areas c and d are generally yellow or green, and most of them have an FUI higher than 10. Since the higher the FUI, the yellower the water color, the water bodies in the selected Tibetan region are generally bluer than those in the Yangtze River and Ganjiang River Basins.

C. Spatial Patterns in the Color of Lakes Across China

In Section III-C, we described how the lakes were divided into eight different groups based on their areas. In Fig. 7, the details of the FUI results for the lakes in each group and their locations are shown. It can be seen that about half (about 49%) of the lakes in China are yellow ($\text{FUI} \geq 13$) and about 41% are green ($9 \leq \text{FUI} < 13$), whereas blue ($1 \leq \text{FUI} < 6$) and cyan ($6 \leq \text{FUI} < 9$) lakes are relatively rare (making up about 3% and 7% of lakes, respectively). Looking at small lakes (area $< 1 \text{ km}^2$) in more detail [see Fig. 7(a) and (b)], the number of small lakes is 57379, which accounts for about 96% of the lakes extracted within China. In addition, only about 9% ($N = 5165$) of these small lakes have FUI values less than 9. This means that there are very few small lakes in China that are blue or cyan. By contrast, the proportion of blue and cyan lakes among large lakes (area $> 1 \text{ km}^2$) is much greater than the corresponding proportion among small water bodies. As for large lakes with areas $> 1 \text{ km}^2$ [see Fig. 7(c)–(h)], the blue and cyan lakes account for the vast majority (about 83%) of the group with areas between 500 and 1000 km^2 [see Fig. 7(g)]; this is followed by the 100 to 500 km^2 group (about 64%) [see Fig. 7(f)], the 50 to 100 km^2 group (about 52%) [see Fig. 7(e)], the 1000 to 5000 km^2 group (about 40%) [see Fig. 7(h)], the 10 to 50 km^2 group (about 31%) [see Fig. 7(d)], and the 1 to 10 km^2 group (about 13%) [see Fig. 7(c)]. In summary, it can be seen that, with the exception of the group with areas between 1000 and 5000 km^2 (which consists of only 10 lakes), the larger the lake area, the greater the proportion of blue and cyan lakes.

In terms of spatial patterns [see Fig. 7(a) and (b)], it can be seen that the small cyan and blue lakes are mainly concentrated in the middle and lower reaches of the Yangtze River and the southeast of the Qinghai–Tibet Plateau; the green ones are mainly

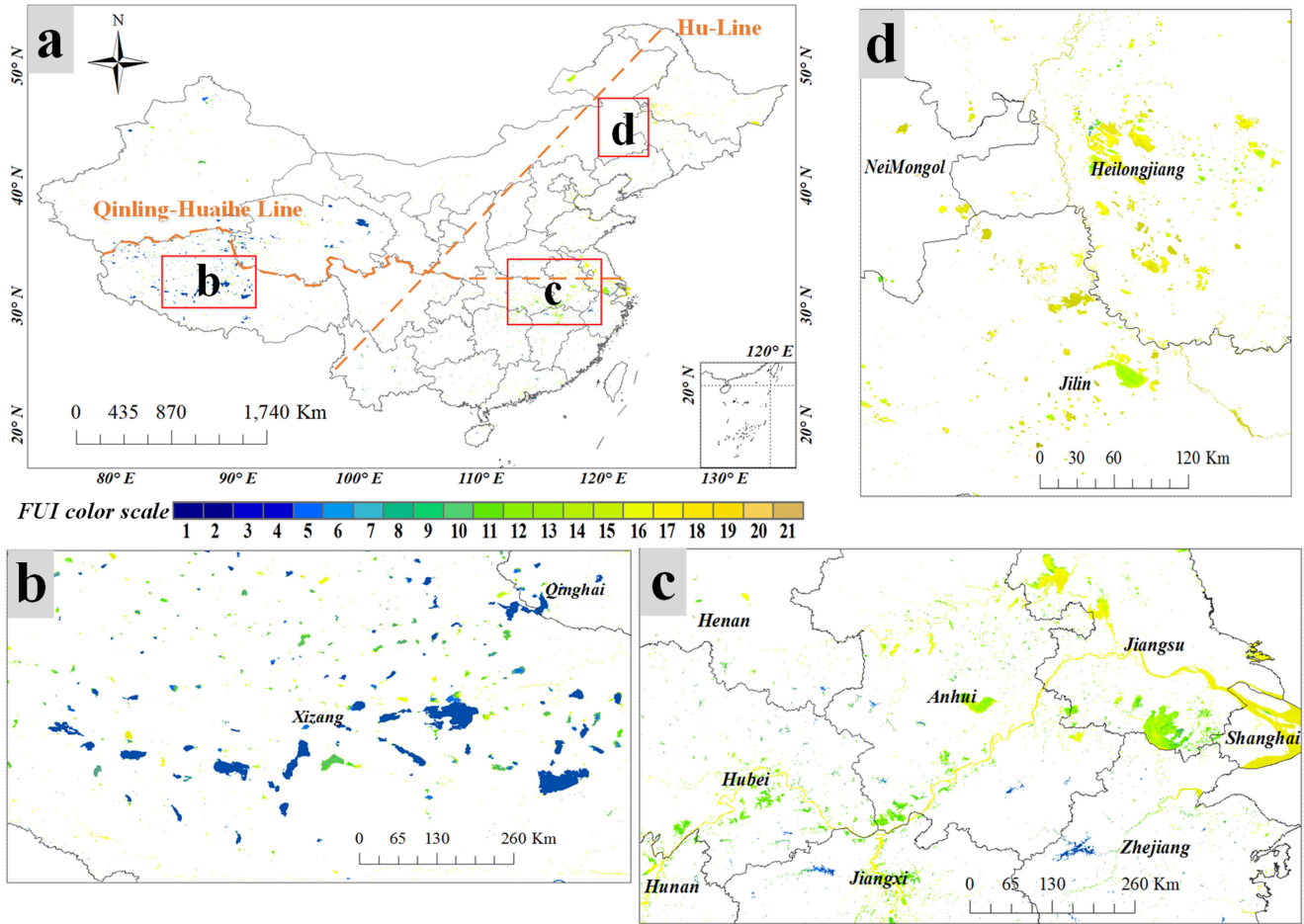


Fig. 6. Chinese FUI water color product for 2015. Typical regions containing water bodies in (b) Tibet, (c) the Yangtze River Basin, and (d) the Ganjiang River Basin. Province names are marked in b, c, and d. The North–South dashed line is the Hu line; the East–West dashed line is the Qinling–Huaihe line.

distributed across the North China Plain, the Yangtze River Plain, and the Qinghai–Tibet Plateau; and the yellow ones are mainly concentrated in the Northeast Plain, Inner Mongolia, and the Qinghai–Tibet Plateau, which are all arid or semiarid regions. Meanwhile, from the distribution patterns of large lakes, most of the blue and cyan lakes are found on the Qinghai–Tibet Plateau and the Yunnan–Guizhou Plateau, whereas the distribution of the large green and yellow lakes is similar to that of the small green and yellow lakes.

In order to further analyze the distribution pattern of the color of lakes in China, China was divided into five limnetic regions (see Fig. 8) [49] based on geological origin, topography, and hydrological characteristic. The five regions were the Northeast Mountain–Plain Region (NER), East Plain Region (EPR), Yungui Plateau Region (YGR), Qinghai–Tibet Plateau Region (QTR), and Mengxin Plateau Region (MXR). We found that about 52%, 21%, 13%, 8%, and 5% of small lakes with areas between 0.01 and 1 km² are located in QTR, EPR, MXR, NER, and YGR, respectively. In addition, most of the small lakes in the QTR, MXR, and NER are yellow lakes ($FUI \geq 13$), accounting for about 64%, about 57%, and about 57% of the lakes in these regions. In contrast, most small lakes in the EPR and YGR

are green—about 83% and about 51%, respectively. The region where blue and cyan lakes make up the highest proportion of small lakes is the YGR, where about 27% of small lakes are in this category. In the QTR, MXR, EPR, and NER, blue and cyan lakes account for about 12%, about 7%, about 4%, and less than 1% of small lakes. The NER has the largest proportion (about 64%) of lakes with areas >1 km² that are yellow among the five regions, the EPR has the largest proportion of green lakes (about 92%), and the YGR has the largest proportion of blue and cyan lakes (about 40%).

As for large lakes with areas >1 km², yellow lakes account for the most in the NER (about 64%), while most of the large lakes in the EPR, YGR, QTR, and MXR are green lakes ($9 \leq FUI < 13$), accounting for about 92%, about 51%, and about 38% of the lakes in these regions. Besides, the region where blue and cyan lakes account for the highest proportion of large lakes is the YGR (40); this is followed by the QTR (34%), the MXR (12%), the EPR (6%), and the NER (less than 1%).

In summary, regardless of the size of lakes, blue and cyan lakes are all mainly concentrated in the YGR and QTR, whereas blue and cyan lakes make up the lowest proportion in EPR and NER.

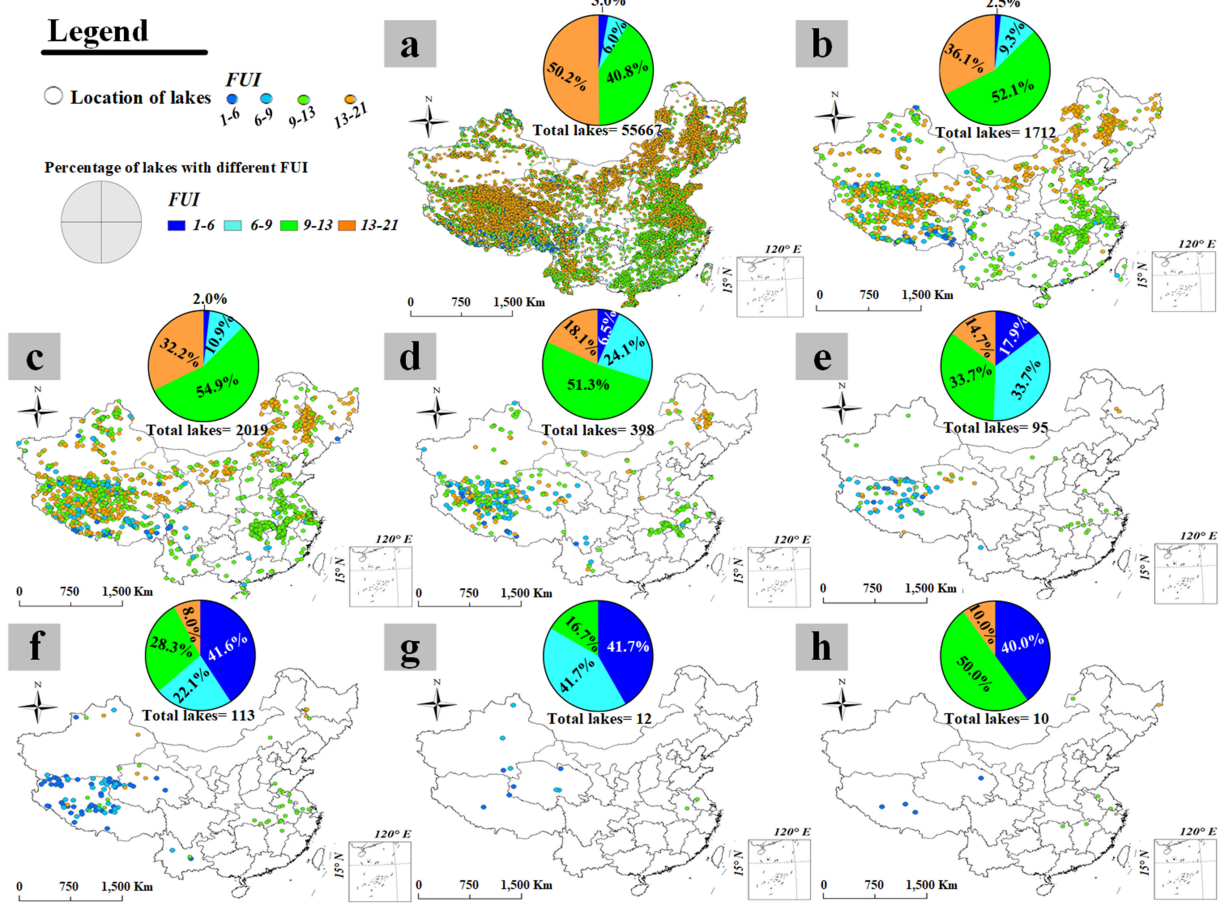


Fig. 7. Spatial patterns in the FUI of lakes in China shown using colored bins. The locations of lakes with areas in the following ranges are shown: (a) 0.01 to 0.5 km², (b) 0.5 to 1 km², (c) 1 to 10 km², (d) 10 to 50 km², (e) 50 to 100 km², (f) 100 to 500 km², (g) 500 to 1000 km², and (h) more than 1000 km². Note that FUI 1–6 indicates $1 \leq \text{FUI} < 6$, FUI 6–9 indicates $6 \leq \text{FUI} < 9$, FUI 9–13 indicates $9 \leq \text{FUI} < 13$, and FUI 13–21 indicates $13 \leq \text{FUI} \leq 21$.

V. DISCUSSION

A. Comparison With the MODIS-Derived FUI Product

Although we used *in situ* measurements to validate our Landsat 8-derived FUI product, the size of these datasets was still limited. In order to further validate the reliability of our product, the MODIS-derived FUI products from June to September 2015 developed by Wang *et al.* [36] were also acquired (see Section II-B). The mean values of these MODIS-derived FUI products were calculated and compared with our Landsat 8-derived FUI data. Fig. 9 shows the results of a comparison of a total of 72495 pairs of water pixels, and it can be seen that most of the scatter points are located close to the 1:1 line. The two products show a high degree of consistency, with an R^2 of 0.90 and a P -value < 0.001 for the relationship. The results shown in Figs. 5 and 9, thus, confirm the reliability of our FUI product to assess water color.

B. Advantages of Using 30-m Landsat 8 Imagery and the GEE Platform to Assess Water Color

In this article, we developed the first 30-m FUI water color product for China by using 30-m Landsat 8 imagery in combination with the GEE platform. Because of the fine spatial resolution of Landsat images, the color of smaller water bodies

can be monitored as well as the color of water bodies with areas greater than 1 km². This was impossible in previous studies that used MODIS and Ocean and Land Color Instrument imagery as the main datasets. Fig. 10 shows the Landsat 8- and MODIS-derived FUI results for four typical regions. The textures of the lakes are clearer at a resolution of 30 m than at 500 m. In addition, the transition in water color from the center to the edge of each lake is much smoother in the 30-m FUI product than in the 500-m one. In addition, from the results for the small water bodies within each region, it can be seen that the color of small water bodies cannot be effectively retrieved from MODIS images, whereas it is well delineated in the FUI results derived from Landsat data. Due to the coarse spatial resolution, more small water bodies are omitted in the MODIS results. The small water bodies that are present in the MODIS results generally have just one FUI value, which makes it impossible to observe the patterns in the FUI within these water bodies. Therefore, the 30-m Landsat 8-derived FUI water color product can provide greater support for the monitoring of water bodies. In addition, by introducing the GEE platform, the huge computing resources and powerful computing capabilities of the GEE make it possible to process massive amounts of Landsat data in a short period of time. Therefore, our research also provides a strategy for quickly assessing water color at a large scale.

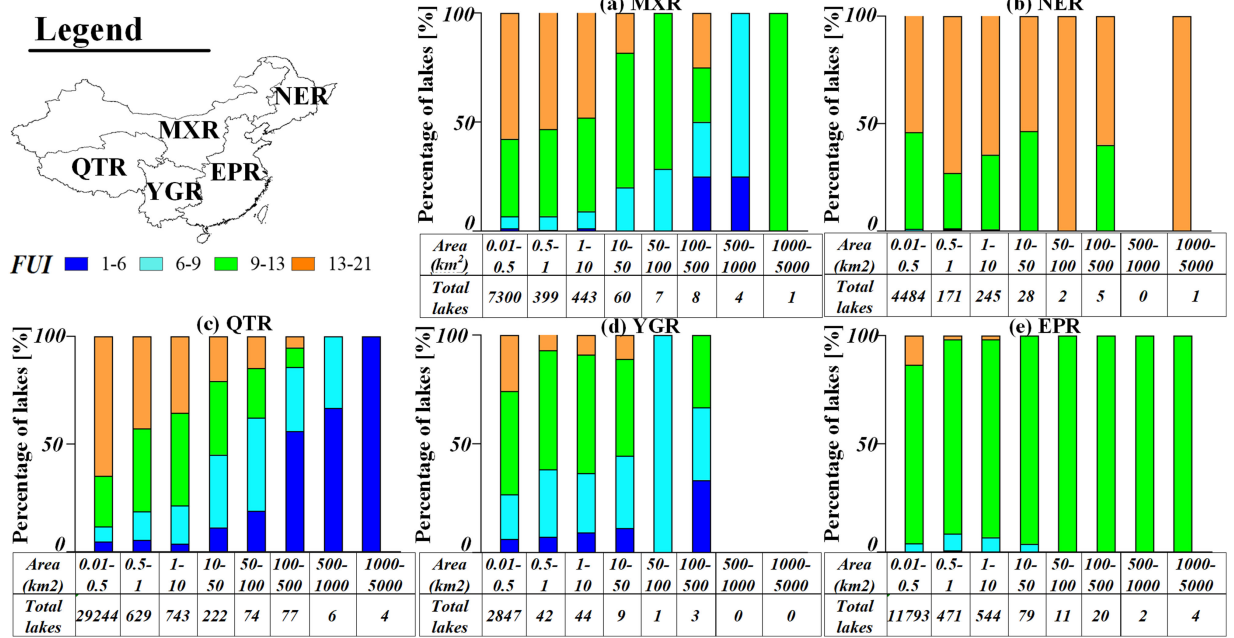


Fig. 8. Percentage distributions of lakes with different FUI values in five limnetic regions. (a)–(e) Statistical results for the MXR, NER, QTR, YGR, and EPR, respectively. Note that FUI 1–6 indicates $1 \leq \text{FUI} < 6$, FUI 6–9 indicates $6 \leq \text{FUI} < 9$, FUI 9–13 indicates $9 \leq \text{FUI} < 13$, and FUI 13–21 indicates $13 \leq \text{FUI} \leq 21$.

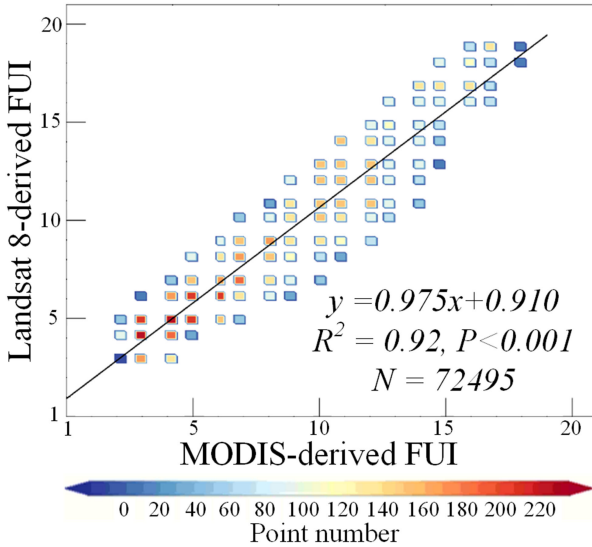


Fig. 9. Scatterplot ($N = 72495$) of our Landsat 8-derived FUI product against the MODIS-derived FUI product.

C. Effectiveness of Using the BAP Algorithm to Derive the Summer Season Composite

In this article, the cloud-free composite that represented the water conditions in summer was generated using the BAP algorithm. In order to demonstrate the effectiveness of the derivation of the composite, the number of valid observations in summer (June to September) was counted and is shown in Fig. 11(a). From Fig. 11(a), except for a few pixels in the southwest of China, the number of the valid observations (noncloud and non-cloud shadow) for most pixels was greater than 5 in the period

covered by the summers of 2014–2016. Therefore, for most locations, the number of valid observations made in summer is sufficient for forming a composite.

In addition, due to the DOY rules for making the BAP composite, the valid observation closest to the target DOY (1 August in this article) is preferentially selected for making the composite. Therefore, compared with other compositing algorithms (such as the median composite and percentile composite algorithms), the BAP has the advantage of generating the most phenologically consistent cloud-free composites [58]. From Fig. 11(b), it can be seen that, for most of the pixels in the generated composite, the observations were made in July and August. Therefore, the composited image produced in this article can effectively represent the water color in summer and ensure the consistency of the phenology.

D. Limitations

First, limited by the revisit period of Landsat 8 and cloud contamination, our method is not suitable for monitoring the continuous variations in water quality throughout the year. In the future, more efforts will be toward the analysis of the use of multisource data to increase the number of valid observations.

Second, the impact of the bottom reflectance may affect the observed color of water bodies, and this situation generally occurs in optical shallow waters. Due to the shallow depths, the signals from the sediment and vegetation at the bottom of water could also contribute to the reflectance out of the water [75]. Although by using only the permanent water area for mapping and adopting the method used in Shen *et al.* [72] to remove the shallow near-shore areas (see Section III) can reduce the interference caused by the shallow pixels, it is almost impossible

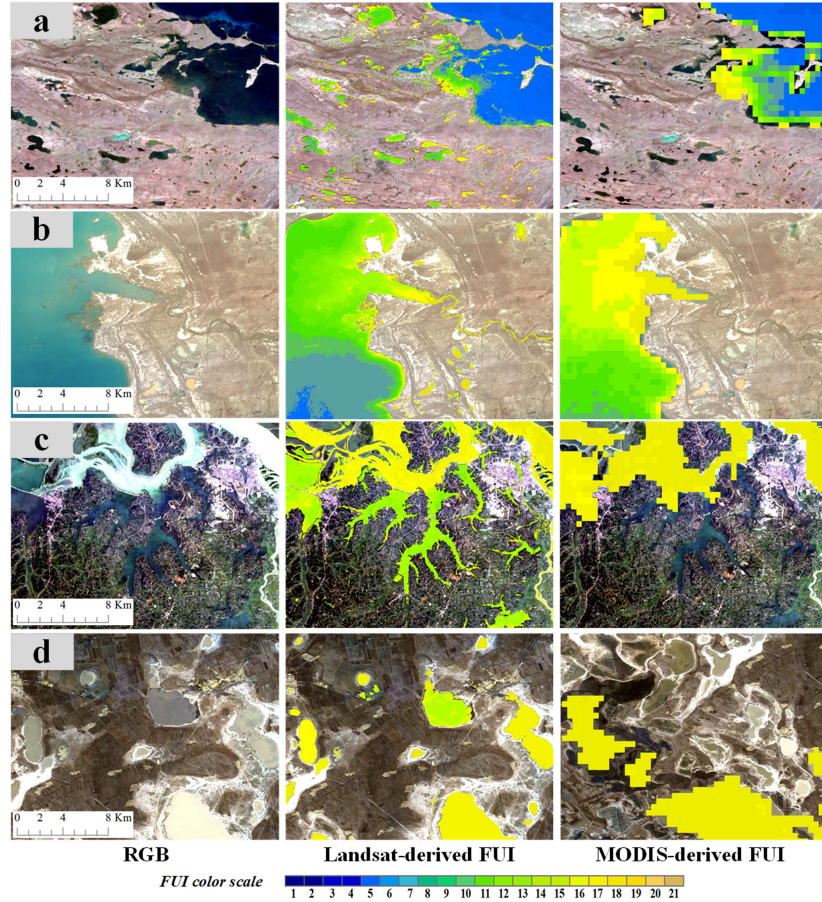


Fig. 10. Comparison between the 30-m Landsat 8-derived FUI product and the 500-m MODIS-derived FUI product. The area shown in (a) is located in Qinghai province (90.1° – 90.4° E, 34.6° – 34.8° N), (b) is in Tibet (89.0° – 89.2° E, 31.9° – 32.1° N), (c) is in Hunan province (112.2° – 112.4° E, 28.7° – 28.9° N), and (d) is in Heilongjiang province (124.4° – 124.7° E, 46.0° – 46.18° N).

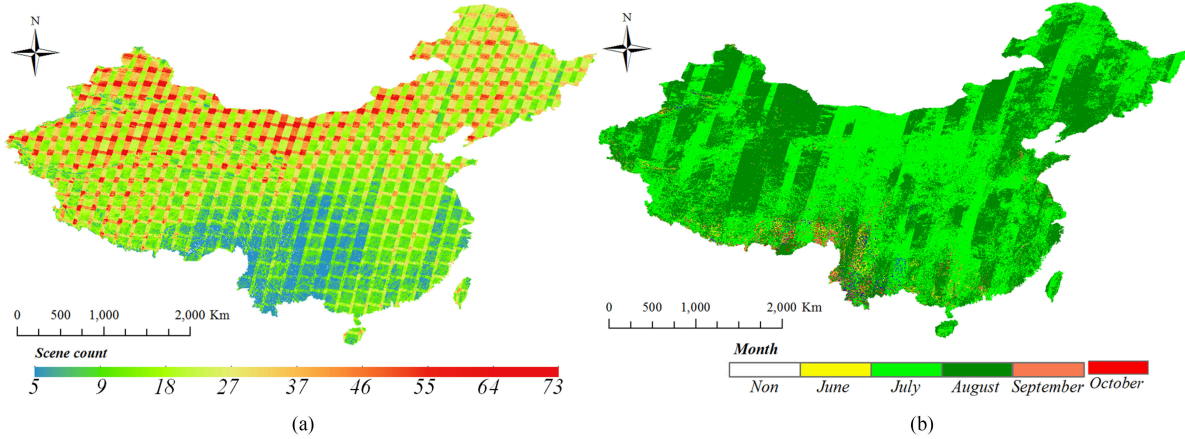


Fig. 11. Number of valid observations and the month in which the data were acquired for each pixel in the BAP composite. (a) Number of valid observations (pixels without cloud or cloud shadow) made at each location from June to September. (b) Month that the data for each pixel in the BAP composite was acquired.

to completely remove the impact of the bottom signal on shallow waters' color. Because the spectral reflectance of the shallow water may be mixed with vegetation or soil land types, there is no method that can accurately classify shallow pixels at a large scale [23]. In the following, we will focus on the method of identifying the optically shallow waters.

VI. CONCLUSION

In this article, the first 30-m FUI water color product for China was developed using Landsat 8 imagery and the GEE cloud computing platform. The generated water color product was shown to have a high degree of consistency with the *in*

situ water SR-derived FUI ($R^2 = 0.90, P < 0.001$). In addition, it also showed a high degree of consistency with the *in situ* SD ($R^2 = 0.89, P < 0.001$) and TLI ($R^2 = 0.77, P < 0.001$) datasets. Next, 60026 lakes in China with areas $>0.01 \text{ km}^2$ were extracted based on the existing lake inventories and reservoir datasets, and the generated FUI product was used to produce the first national assessment of the color of lakes with areas $>0.01 \text{ km}^2$. The results indicated that overall, the FUI values of the water bodies showed a marked spatial pattern with the values being high in the north and low in the south, as well as high in the east and low in the west. Generally, water bodies to the north and south of the Qinlin–Huaihe line had FUI values of about 11.0 and 10.5, respectively; water bodies to the east and west of the Hu Line had FUI values larger than 12 and around 10.5, respectively. In addition, most lakes in China are yellow (about 49%) or green (about 41%), while blue (about 3%) and cyan (about 7%) lakes are relatively rare. Also, a much larger proportion of small lakes with areas $< 1 \text{ km}^2$ are yellow than are large lakes with areas $> 1 \text{ km}^2$. About 50% ($N = 28569$) of small lakes are yellow, whereas yellow lakes only account for 29% ($N = 737$) and 7% ($N = 10$) of large lakes with areas in the ranges 1 km^2 to 100 km^2 and greater than 100 km^2 , respectively. Moreover, in terms of spatial patterns, blue and cyan lakes are mainly concentrated in the YGR and QTR, whereas blue and cyan lakes make up the lowest proportion in EPR and NER. This 30-m FUI water color product for China will be extremely important to the preservation and restoration of inland water bodies. This article will be extended to even broader spatial–temporal scales in the future.

Data Availability: Our 30-m Landsat 8-derived FUI product for China and the generated 2015 Chinese lake database that was generated are now available for free download at <https://zenodo.org/record/4280871> and <https://zenodo.org/record/4280859>, respectively.

REFERENCES

- [1] S. L. Postel, “Entering an era of water scarcity: The challenges ahead,” *Ecological Appl.*, vol. 10, no. 4, pp. 941–948, Aug. 2000.
- [2] J. Li *et al.*, “MODIS observations of water color of the largest 10 lakes in china between 2000 and 2012,” *Int. J. Digit. Earth*, vol. 9, no. 8, pp. 788–805, Apr. 2016.
- [3] S. Wang, J. Li, Q. Shen, B. Zhang, F. Zhang, and Z. Lu, “MODIS-Based radiometric color extraction and classification of inland water with the forel-ule scale: A case study of lake taihu,” *IEEE J. Sel. Topics Appl. Earth Observ. Remote Sens.*, vol. 8, no. 2, pp. 907–918, Feb. 2015.
- [4] X. Wang and W. Yang, “Water quality monitoring and evaluation using remote-sensing techniques in china: A systematic review,” *Ecosystem Health Sustainability*, vol. 5, no. 1, pp. 47–56, Jan. 2019.
- [5] H. Ma, J. Xu, and P. Wang, “Water resource utilization and china’s urbanization,” *Resour. Sci.*, vol. 36, no. 2, pp. 334–341, 2014.
- [6] Ministry of Ecology and Environment of the People’s Republic of China, “A picture of speed reading 2017 china’s ecological environment bulletin,” May 2018. [Online]. Available: http://www.zhb.gov.cn/hjzl/tj/201805/t20180531_442197.shtml
- [7] T. Ma *et al.*, “Pollution exacerbates china’s water scarcity and its regional inequality,” *Nature Commun.*, vol. 11, no. 1, pp. 1–9, Jan. 2020.
- [8] J. C. Huang *et al.*, “How successful are the restoration efforts of china’s lakes and reservoirs?” *Environ. Int.*, vol. 123, pp. 96–103, Feb. 2019.
- [9] R. Fatima, “Studies on physical, chemical and bacteriological characteristics on quality of spring water in Hajigak iron ore mine, Bamyan province, central Afghanistan,” *Open J. Geol.*, vol. 8, pp. 313–332, Mar. 2018.
- [10] N. Diersing, *Water Quality: Frequently Asked Questions*. Key West, FL, USA: Florida Brooks National Marine Sanctuary, 2009.
- [11] J. Ritchie, P. Zimba, and J. Everitt, “Remote sensing techniques to assess water quality,” *Photogrammetric Eng. Remote Sens.*, vol. 69, no. 6, Jun. 2003.
- [12] A. P. Trishchenko, J. Cihlar, and Z. Q. Li, “Effects of spectral response function on surface reflectance and NDVI measured with moderate resolution satellite sensors,” *Remote Sens. Environ.*, vol. 81, no. 1, pp. 1–18, Jul. 2002.
- [13] F. Zhang *et al.*, “Validation of a synthetic chlorophyll index for remote estimates of chlorophyll-a in a turbid hypereutrophic lake,” *Int. J. Remote Sens.*, vol. 35, no. 1, pp. 289–305, Jan. 2014.
- [14] H. J. van der Woerd and M. R. Wernand, “Hue-Angle product for low to medium spatial resolution optical satellite sensors,” *Remote Sens.*, vol. 10, no. 2, Feb. 2018.
- [15] J. Li *et al.*, “Retrieving total suspended matter in lake taihu from HJ-CCD near-infrared band data,” *Aquatic Ecosystem Health Manage.*, vol. 17, no. 3, pp. 280–289, Jul.–Sep. 2014.
- [16] H. Duan, R. Ma, and C. Hu, “Evaluation of remote sensing algorithms for cyanobacterial pigment retrievals during spring bloom formation in several lakes of east china,” *Remote Sens. Environ.*, vol. 126, pp. 126–135, Nov. 2012.
- [17] P. L. Brezonik *et al.*, “Factors affecting the measurement of CDOM by remote sensing of optically complex inland waters,” *Remote Sens. Environ.*, vol. 157, pp. 199–215, Feb. 2015.
- [18] M. Tao, H. T. Duan, Z. G. Cao, S. A. Loiselle, and R. Ma, “A hybrid EOF algorithm to improve MODIS cyanobacteria phycocyanin data quality in a highly turbid lake: Bloom and nonbloom condition,” *IEEE J. Sel. Topics Appl. Earth Observ. Remote Sens.*, vol. 10, no. 10, pp. 4430–4444, Oct. 2017.
- [19] H. T. Duan *et al.*, “MODIS observations of cyanobacterial risks in a eutrophic lake: Implications for long-term safety evaluation in drinking-water source,” *Water Res.*, vol. 122, pp. 455–470, Oct. 2017.
- [20] R. E. Carlson, “trophic state index for lakes,” *Limnol. Oceanogr.*, vol. 22, no. 2, pp. 361–369, Mar. 1977.
- [21] C. Le *et al.*, “A four-band semi-analytical model for estimating chlorophyll a in highly turbid lakes: The case of taihu lake, china,” *Remote Sens. Environ.*, vol. 113, no. 6, pp. 1175–1182, Jun. 2009.
- [22] E. Spyarakos *et al.*, “Optical types of inland and coastal waters,” *Limnol. Oceanogr.*, vol. 63, no. 2, pp. 846–870, Mar. 2018.
- [23] S. Wang *et al.*, “Trophic state assessment of global inland waters using a MODIS-derived forel-ule index,” *Remote Sens. Environ.*, vol. 217, pp. 444–460, Nov. 2018.
- [24] P. Ylostalo, K. Kallio, and J. Seppala, “Absorption properties of in-water constituents and their variation among various lake types in the boreal region,” *Remote Sens. Environ.*, vol. 148, pp. 190–205, May 2014.
- [25] S. C. J. Palmer, T. Kutser, and P. D. Hunter, “Remote sensing of inland waters: Challenges, progress and future directions,” *Remote Sens. Environ.*, vol. 157, pp. 1–8, Feb. 2015.
- [26] C. B. Mouw *et al.*, “Aquatic color radiometry remote sensing of coastal and inland waters: Challenges and recommendations for future satellite missions,” *Remote Sens. Environ.*, vol. 160, pp. 15–30, Apr. 2015.
- [27] M. R. Wernand, H. J. van der Woerd, and W. W. C. Gieskes, “Trends in ocean colour and chlorophyll concentration from 1889 to 2000, worldwide,” *Plos One*, vol. 8, no. 6, Jun. 2013, Art. no. e63766.
- [28] J. A. Busch *et al.*, “Citizen bio-optical observations from Coast- and Ocean and their compatibility with ocean colour satellite measurements,” *Remote Sens.*, vol. 8, no. 11, Nov. 2016, Art. no. 879.
- [29] S. P. Garaba *et al.*, “Using ocean colour remote sensing products to estimate turbidity at the wadden sea time series station spiekeroog,” *J. Eur. Opt. Soc.-Rapid Pub.*, vol. 9, Jun. 2014, Art. no. 14020.
- [30] A. Forel, “Une nouvelle forme de la gamme de couleur pour l’étude de l’eau des lacs,” in *Archives Des Sciences, Physiques Et Naturelles*, vol. 6, p. 25, 1890.
- [31] W. Ule, “Die bestimmung der wasserfarbe in den seen,” in *Petermanns Mittheilungen aus Justus Perthes Geographischer Anstalt*, Gotha, Germany: Justus Perthes, 1892, pp. 70–71.
- [32] M. R. Wernand and H. J. van der Woerd, “Spectral analysis of the forel-ule ocean colour comparator scale,” *J. Eur. Opt. Soc.-Rapid Pub.*, vol. 5, Apr. 2010, Art. no. 100014s.
- [33] H. J. van der Woerd and M. R. Wernand, “True colour classification of natural waters with medium-spectral resolution satellites: SeaWiFS, MODIS, MERIS and OLCI,” *Sensors*, vol. 15, no. 10, pp. 25663–25680, Oct. 2015.
- [34] M. R. Wernand, A. Hommersom, and H. J. van der Woerd, “MERIS-based ocean colour classification with the discrete forel-ule scale,” *Ocean Sci.*, vol. 9, no. 3, pp. 477–487, May 2013.

- [35] J. Pitarch *et al.*, "Optical properties of fore-ule water types deduced from 15 years of global satellite ocean color observations," *Remote Sens. Environ.*, vol. 231, Sep. 2019, Art. no. 111249.
- [36] S. Wang *et al.*, "Changes of water clarity in large lakes and reservoirs across china observed from long-term MODIS," *Remote Sens. Environ.*, vol. 247, Sep. 2020, Art. no. 111949.
- [37] Q. Chen, M. Huang, and X. Tang, "Eutrophication assessment of seasonal urban lakes in china yangtze river basin using landsat 8-derived fore-ule index: A six-year (2013-2018) observation," *Sci. total Environ.*, vol. 745, Nov. 2020, Art. no. 135392.
- [38] N. Gorelick *et al.*, "Google earth engine: Planetary-scale geospatial analysis for everyone," *Remote Sens. Environ.*, vol. 202, pp. 18–27, Dec. 2017.
- [39] S. N. Kloiber *et al.*, "A procedure for regional lake water clarity assessment using landsat multispectral data," *Remote Sens. Environ.*, vol. 82, no. 1, pp. 38–47, Sep. 2002.
- [40] I. M. McCullough, C. S. Loftin, and S. A. Sader, "Combining lake and watershed characteristics with landsat TM data for remote estimation of regional lake clarity," *Remote Sens. Environ.*, vol. 123, pp. 109–115, Aug. 2012.
- [41] S. P. Singh and P. Singh, "Effect of temperature and light on the growth of algae species: A review," *Renewable Sustain. Energy Rev.*, vol. 50, pp. 431–444, Oct. 2015.
- [42] G. Zhang *et al.*, "Regional differences of lake evolution across china during 1960s-2015 and its natural and anthropogenic causes," *Remote Sens. Environ.*, vol. 221, pp. 386–404, Feb. 2019.
- [43] J. Yu *et al.*, "Developing daily cloud-free snow composite products from MODIS terra-aqua and IMS for the tibetan plateau," *IEEE Trans. Geosci. Remote Sens.*, vol. 54, no. 4, pp. 2171–2180, Apr. 2016.
- [44] E. Vermote *et al.*, "Preliminary analysis of the performance of the landsat 8/OLI land surface reflectance product," *Remote Sens. Environ.*, vol. 185, pp. 46–56, Nov. 2016.
- [45] Z. Zhu, S. Wang, and C. E. Woodcock, "Improvement and expansion of the fsmask algorithm: Cloud, cloud shadow, and snow detection for landsats 4–7, 8, and sentinel 2 images," *Remote Sens. Environ.*, vol. 159, pp. 269–277, Mar. 2015.
- [46] X. Chen, L. Liu, X. Zhang, S. Xie, and L. Lei, "A novel water change tracking algorithm for dynamic mapping of inland water using time-series remote sensing imagery," *IEEE J. Sel. Topics Appl. Earth Observ. Remote Sens.*, vol. 13, pp. 1661–1674, Apr. 2020.
- [47] J. Liu *et al.*, "Mapping paddy rice in jiangsu province, china, based on phenological parameters and a decision tree model," *Front. Earth Sci.*, vol. 13, no. 1, pp. 111–123, Mar. 2019.
- [48] R. Ma *et al.*, "Detecting aquatic vegetation changes in taihu lake, china using Multi-temporal satellite imagery," *Sensors*, vol. 8, no. 6, pp. 3988–4005, Jun. 2008.
- [49] R. Ma *et al.*, "China's lakes at present: Number, area and spatial distribution," *Sci. China-Earth Sci.*, vol. 54, no. 2, pp. 283–289, Feb. 2011.
- [50] K. Song *et al.*, "Quantification of lake clarity in china using landsat OLI imagery data," *Remote Sens. Environ.*, vol. 243, Jun. 2020, Art. no. 111800.
- [51] B. Lehner and P. Doll, "Development and validation of a global database of lakes, reservoirs and wetlands," *J. Hydrol.*, vol. 296, no. 1–4, pp. 1–22, Aug. 2004.
- [52] K. Song *et al.*, "Dissolved carbon in a large variety of lakes across five limnetic regions in china," *J. Hydrol.*, vol. 563, pp. 143–154, Aug. 2018.
- [53] R. P. Bukata *et al.*, "Validation of a radiometric color model applicable to optically complex water bodies," *Remote Sens. Environ.*, vol. 77, no. 2, pp. 165–172, Aug. 2001.
- [54] D. Wang *et al.*, "The assessment of landsat-8 OLI atmospheric correction algorithms for inland waters," *Remote Sens.*, vol. 11, no. 2, Jan. 2019, Art. no. 169.
- [55] D. Liu *et al.*, "Observations of water transparency in china's lakes from space," *Int. J. Appl. Earth Observ. Geoinformation*, vol. 92, Oct. 2020, Art. no. 102087.
- [56] J. C. White *et al.*, "Pixel-Based image compositing for large-area dense time series applications and science," *Can. J. Remote Sens.*, vol. 40, no. 3, pp. 192–212, Aug. 2014.
- [57] P. Beckschaefer, "Obtaining rubber plantation age information from very dense landsat TM & ETM plus time series data and pixel-based image compositing," *Remote Sens. Environ.*, vol. 196, pp. 89–100, Jul. 2017.
- [58] P. Griffiths, S. van der Linden, T. Kuemmerle, and P. Hostert, "Pixel-Based landsat compositing algorithm for large area land cover mapping," *IEEE J. Sel. Topics Appl. Earth Observ. Remote Sens.*, vol. 6, no. 5, pp. 2088–2101, Oct. 2013.
- [59] D. K. Bolton *et al.*, "Optimizing landsat time series length for regional mapping of lidar-derived forest structure," *Remote Sens. Environ.*, vol. 239, Mar. 2020, Art. no. 111645.
- [60] T. Hermosilla *et al.*, "An integrated landsat time series protocol for change detection and generation of annual gap-free surface reflectance composites," *Remote Sens. Environ.*, vol. 158, pp. 220–234, Mar. 2015.
- [61] J. C. White *et al.*, "A nationwide annual characterization of 25 years of forest disturbance and recovery for Canada using landsat time series," *Remote Sens. Environ.*, vol. 194, pp. 303–321, Jun. 2017.
- [62] C. Gomez, J. C. White, and M. A. Wulder, "Optical remotely sensed time series data for land cover classification: A review," *ISPRS J. Photogrammetry Remote Sens.*, vol. 116, pp. 55–72, Jun. 2016.
- [63] P. Griffiths *et al.*, "Forest disturbances, forest recovery, and changes in forest types across the carpathian ecoregion from 1985 to 2010 based on landsat image composites," *Remote Sens. Environ.*, vol. 151, pp. 72–88, Aug. 2014.
- [64] T. Arvidson, J. Gasch, and S. N. Goward, "Landsat 7's long-term acquisition plan - an innovative approach to building a global imagery archive," *Remote Sens. Environ.*, vol. 78, no. 1/2, pp. 13–26, Oct. 2001.
- [65] S. K. McFeeters, "The use of the normalized difference water index (NDWI) in the delineation of open water features," *Int. J. Remote Sens.*, vol. 17, no. 7, pp. 1425–1432, May 1996.
- [66] S. Novoa, M. R. Wernand, and H. J. van der Woerd, "The forel-ule scale revisited spectrally: Preparation protocol, transmission measurements and chromaticity," *J. Eur. Opt. Soc.-Rapid Pub.*, vol. 8, Aug. 2013, Art. no. 13057.
- [67] CIE, *Commission Internationale de L'éclairage Proceedings*. Cambridge, U.K.: Cambridge Univ. Press, 1932.
- [68] S. Wang, *Large-scale and Long-time Water Quality Remote Sensing Monitoring Over Lakes Based On Water Color Index*, Beijing, China: Univ. Chinese Academy Sci., 2018.
- [69] Y. Dai *et al.*, "An automatic classification algorithm for submerged aquatic vegetation in shallow lakes using landsat imagery," *Remote Sens. Environ.*, vol. 260, Jul. 2021, Art. no. 112459.
- [70] C. Hu, "A novel ocean color index to detect floating algae in the global oceans," *Remote Sens. Environ.*, vol. 113, no. 10, pp. 2118–2129, Oct. 2009.
- [71] J. Ma *et al.*, "Spatio-Temporal variations and driving forces of harmful algal blooms in chaohu lake: A multi-source remote sensing approach," *Remote Sens.*, vol. 13, no. 3, pp. 427, Feb. 2021.
- [72] M. Shen *et al.*, "Sentinel-3 OLCI observations of water clarity in large lakes in eastern china: Implications for SDG 6.3.2 evaluation," *Remote Sens. Environ.*, vol. 247, Sep. 2020, Art. no. 111950.
- [73] H. Hu, "Population distribution, regionalization, and prospects in china," *Acta Geographica Sinica*, vol. 45, no. 2, pp. 139–145, Jun. 1990.
- [74] Y. Liu, C. Chen, and Y. Li, "Differentiation regularity of urban-rural equalized development at prefecture-level city in china," *J. Geographical Sci.*, vol. 25, no. 9, pp. 1075–1088, Sep. 2015.
- [75] L. Feng, X. Hou, and Y. Zheng, "Monitoring and understanding the water transparency changes of fifty large lakes on the yangtze plain based on long-term MODIS observations," *Remote Sens. Environ.*, vol. 221, pp. 675–686, Feb. 2019.



Xidong Chen received the B.S. degree in remote sensing science and technology from Henan Polytechnic University, Jiaozuo, China. He is currently working toward the Ph.D. degree in vegetation quantitative remote sensing with the Aerospace Information Research Institute, Chinese Academy of Sciences, Beijing, China.

His research interests include quantitative remote sensing of land surfaces and remote sensing classification.



Liangyun Liu received the B.S. degree from Huabei Normal University, Anhui, China, in 1996, and the Ph.D. degree in optics from the Xi'an Institute of Optics and Procession Mechanics, Chinese Academy of Sciences, Xi'an, China, in 2000.

He is currently a Research Professor with the Aerospace Information Research Institute, Chinese Academy of Sciences, Beijing, China. He has authored and coauthored more than 200 journal papers in vegetation quantitative remote sensing.

Dr. Liu was the recipient of five government's prizes, including two second-class National Scientific and Technological Progress Award, and also honored by National Science Fund for Distinguished Young Scholars in 2018.



Dong Liu received the Ph.D. degree in remote sensing science and technology from Zhejiang University, Hangzhou, China.

He is currently with the Nanjing Institute of Geography and Limnology, Chinese Academy of Sciences, Beijing, China. His research interests include ocean color remote sensing, lake carbon cycle, water quality monitoring, etc.



Xiao Zhang received the Ph.D. degree in vegetation quantitative remote sensing from the Aerospace Information Research Institute, Chinese Academy of Sciences, Beijing, China, in 2020.

He is a Research Assistant Professor with the Aerospace Information Research Institute, Chinese Academy of Sciences. His research interests include image processing and time series land cover mapping.



Hongtao Duan was born in Jiaozuo, Henan, China, in 1979. He received the B.S. degree in city planning from Northwest University, Kirkland, WA, USA, in 2002, and the Ph.D. degree in GIS from the University of Chinese Academy of Sciences, Beijing, China, in 2007.

From 2007 to 2009, he was a Research Assistant with the Nanjing Institute of Geography and Limnology, Chinese Academy of Sciences. From 2010 to 2014, he was an Associate Researcher and a Master Supervisor with the Nanjing Institute of Geography and Limnology, Chinese Academy of Sciences. Since 2015, he has been a Researcher and a Doctoral Supervisor with the Nanjing Institute of Geography and Limnology, Chinese Academy of Sciences. His current research interests include remote sensing of ocean color and water environment simulation.

Dr. Duan was an Excellent Graduate of the University of Chinese Academy of Sciences, in 2007, an Excellent Member of the Youth Promotion Association of the Chinese Academy of Sciences, in 2014, and the Young Yangtze River Scholar, in 2019.



Junsheng Li received the Ph.D. degree in remote sensing science from the Institute of Remote Sensing Applications, Chinese Academy of Sciences, Beijing, China, in 2007.

He is currently a Research Professor with the Aerospace Information Research Institute, Chinese Academy of Sciences. His research interests include water color remote sensing, and his current research interests include remote sensing of inland waters, including atmospheric correction, eutrophic state assessment, and water clarity estimation.



Kaishan Song received the M.S. degree in GIS and cartography from Northeast Normal University, Changchun, China, in 2002, and the Ph.D. degree in remote sensing application from the Northeast Institute of Geography and Agricultural Ecology (NEIGAE), Chinese Academy of Sciences, Changchun, in 2005.

From 2005 to 2006 and 2006 to 2011, he was an Assistant Professor and an Associate Professor, respectively, and since 2011, he has been a Full Professor of remote sensing technology and applications with the Remote Sensing Division, NEIGAE. He has authored more than 80 English peer-reviewed journal papers and one book on the spectral characterization of region terrestrial targets in Northeast China. His research interests include inland water bio-optical properties and water quality monitoring with remotely sensed data (e.g., apparent and inherent optical properties of inland productive waters, remote estimation of various water components with both *in situ* and imagery measurements).



Shenglei Wang received the Ph.D. degree in cartography and geographic information system from the University of Chinese Academy of Sciences, Beijing, China, in 2018.

From 2017 to 2019, she was a joint-training Ph.D. student and then a Research Fellow at the Department of Biological and Environmental Science, University of Stirling, U.K. From 2019 to 2020, she was a Postdoctoral Research Fellow with the Peking University, Beijing. She is currently working in Aerospace Information Research Institute, Chinese Academy of Sciences, China. Her research interests include water optical remote sensing, bio-optical properties, and radiative transfer process in optically complex waters.